

DETC99/DAC-8644

A PSEUDO-RIGID-BODY MODEL FOR FUNCTIONALLY BINARY PINNED-PINNED SEGMENTS USED IN COMPLIANT MECHANISMS

Brian T. Edwards

Mechanical Dynamics, Inc.
2301 Commonwealth Blvd.
Ann Arbor, Michigan 48105

Brian D. Jensen

Intelligent Micromachines
Department
Sandia National Laboratories
Albuquerque, New Mexico
87123
bjense@sandia.gov

Larry L. Howell

Mechanical Engineering
Department
Brigham Young University
Provo, Utah 84602
lhowell@et.byu.edu

ABSTRACT

The pseudo-rigid-body model concept allows compliant mechanisms to be analyzed using well-known rigid-body kinematics. This paper presents a pseudo-rigid-body model for initially circular functionally binary pinned-pinned segments that undergo large, nonlinear deflections. The model approximates the functionally binary pinned-pinned segment as three rigid members joined by pin joints. Torsional springs placed at the joints model the segment's stiffness. This model has been tested by fabricating several such segments from a variety of different materials. An example mechanism incorporating functionally binary pinned-pinned segments is also presented.

INTRODUCTION

The nonlinear deflections often associated with the motion of compliant mechanisms increase the complexity of compliant mechanism analysis and design. Though these deflections may be difficult to analyze, they are necessary because many of the advantages of compliant mechanisms result from the reduced part count made possible by obtaining motion from deflections rather than from traditional kinematic pairs (Shoup and McLarnan, 1971; Ananthasuresh and Kota, 1995). Analysis methods must be developed that simplify the analysis of the large-deflection compliant members so that compliant mechanisms may be designed. The pseudo-rigid-body model concept has been developed in response to this need (Howell and Midha, 1994). The pseudo-rigid-body model is used to unify compliant

mechanism theory with rigid-body mechanism theory. This is accomplished by replacing a compliant segment with two or more rigid segments joined by a pin joint, with the lengths of the equivalent rigid segments specified so that their motion closely models that of the compliant segments. A torsional spring at the pin joint models the compliant segment's resistance to bending. This type of model has been applied to small-length flexural segments (Howell and Midha, 1994), initially straight fixed compliant segments with constant end loads (Howell and Midha, 1995), and initially curved segments with similar loads (Howell and Midha, 1996).

Other methods exist as alternatives to the pseudo-rigid-body model for the design of compliant mechanisms. For example, structural optimization, homogenization theory, topology optimization, and multi-criteria optimization methods have been proposed for compliant mechanism design (Ananthasuresh and Kota, 1994, Frecker et al., 1997, Sigmund, 1996).

A common compliant link that has yet to have a pseudo-rigid-body model is the functionally binary pinned-pinned segment (FBPP segment), shown schematically in Fig. 1 (Edwards, 1996). Because it is pinned at both ends, the segment cannot carry moments or vertical loads; it is limited to horizontal loading. Because of this required loading, the segment behaves much like a simple linear spring. However, its force-deflection characteristics are not linear, and they depend to a large extent on the parameters of the FBPP segment. This paper presents a model for finding the force and moment characteristics of segments whose undeflected shape is a circular arc, as shown in

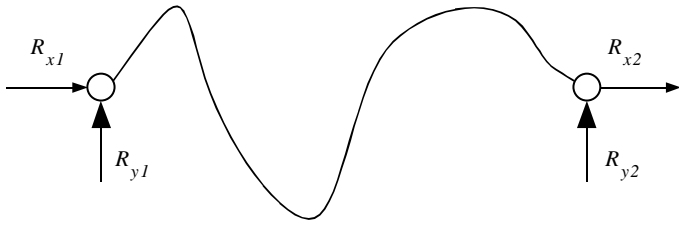


Figure 1: A general functionally binary pinned-pinned (FBPP) segment

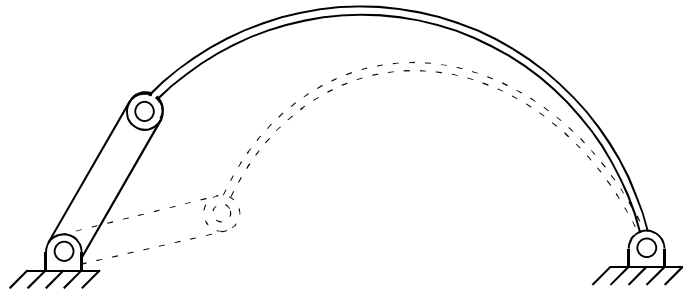


Figure 3: A partially-compliant mechanism using a functionally binary pinned-pinned segment

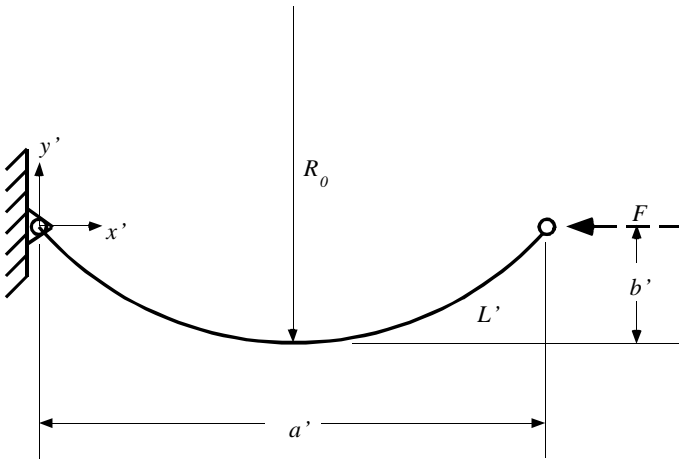


Figure 2: A functionally binary pinned-pinned (FBPP) segment whose shape is a circular arc

Fig. 2. This segment is often used in compliant mechanisms because of its simple geometry. For example, the mechanism illustrated schematically in Fig. 3 uses a functionally binary pinned-pinned segment to allow motion. The model presented in this paper will allow this motion to be analyzed using rigid-body kinematics.

Before analyzing the segment shown in Fig. 2, the problem can be simplified by realizing that the segment is symmetric about a vertical line through its center. This symmetry can be used to divide the complete FBPP segment into two equivalent half-segments. One such half-segment is shown in Fig. 4. This segment will be analyzed, and the results will be generalized to the full segment. The following sections show how this may be done.

ELLIPTIC INTEGRAL SOLUTION

The large-scale force-deflection relationships for functionally binary pinned-pinned (FBPP) segments require some form of a nonlinear solution. The classical method for determining these values has been through the use of elliptic integrals, which provide a means for solving the nonlinear equations (Bisshopp and Drucker, 1945; Frisch-Fay, 1962). Elliptic integrals are any of a wide range of non-elementary

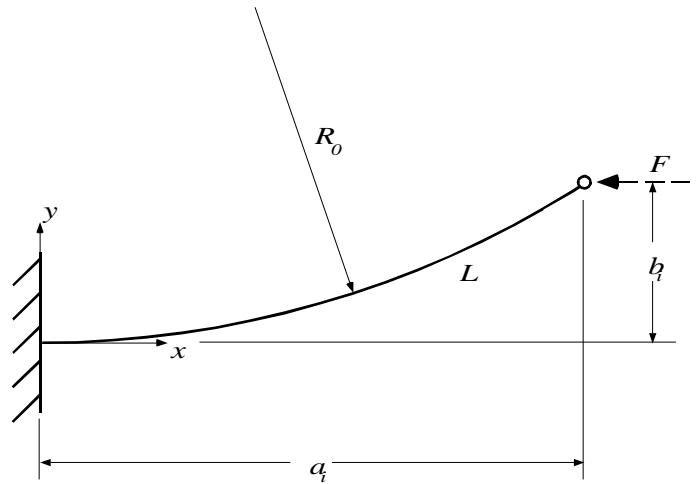


Figure 4: FBFP half-model of FBPP segment

integrals which are intractable and have no elementary solution (Byrd and Friedman, 1954). Integrals which can be manipulated to conform to an elliptic integral basic function can then be transformed into an elliptic integral solution. These solutions may be evaluated using methods such as Landen's scale of increasing amplitudes, which uses Gauss' Arithmetico-Geometrical Means (King, 1924).

Upon deflection, the FBPP segment assumes an unknown shape which varies based on initial curvature, material properties, and applied force. The curvature of the half-segment may be found using the Bernoulli-Euler equation:

$$\frac{1}{R_0} + \frac{M_f(s)}{EI} = \frac{d\theta}{ds} = \frac{\frac{d^2 y}{dx^2}}{\left[1 + \left(\frac{dy}{dx}\right)^2\right]^{3/2}} \quad (1)$$

where R_0 is the initial curvature, $M_f(s)$ is the internal moment at any distance s along the segment, θ is the angle between the segment tangent and the horizontal, and x and y are the coordinates of the beam at a distance s along the segment. Elliptic

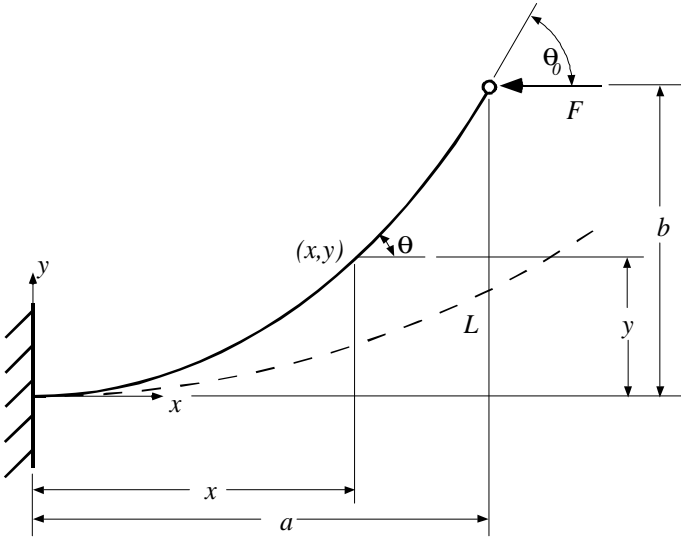


Figure 5: Deflected segment position

integrals provide the means for solving this equation to achieve formulas specifying the horizontal, vertical, and angular positions of the unknown deflected shape. Upon application of a force, the segment shown in Fig. 4 deflects to a new position, as shown in Fig. 5. The x - and y -coordinates of the pin joint in the deflected position are defined as a and b . At any point (x, y) along the segment, the angle between the segment tangent and the x -axis is θ ; at the pin joint, the tangent angle is θ_0 . Applying the Bernoulli-Euler equation gives

$$\kappa = \frac{M_f(s)}{EI} + \frac{1}{R_0} \quad (2)$$

where κ is the curvature in the final deflected position. Since the force F is horizontal, the moment $M_f(s)$ at the point (x, y) is

$$M_f(s) = F(b - y) \quad (3)$$

The curvature k is also defined as the change in the tangent angle θ with respect to the arc distance s , or

$$\kappa = \frac{d\theta}{ds} \quad (4)$$

Substituting Eqs. (3) and (4) into Eq. (2) and differentiating with respect to s gives

$$\frac{d^2\theta}{ds^2} = \frac{-F dy}{EI ds} \quad (5)$$

It is necessary to express Eq. (5) in terms of κ instead of θ . Equation (5) can also be written as

$$\frac{d^2\theta}{ds^2} = \frac{d}{d\theta} \left(\frac{d\theta}{ds} \right) \frac{d\theta}{ds} = \frac{d\kappa}{d\theta} \kappa = \frac{d}{d\theta} \left(\frac{\kappa^2}{2} \right) \quad (6)$$

In addition, when moving an infinitesimal distance ds along the curve, the following relationships apply:

$$\frac{dx}{ds} = \cos\theta \quad (7)$$

$$\frac{dy}{ds} = \sin\theta \quad (8)$$

Substituting both Eqs. (6) and (8) into Eq. (5) results in

$$\frac{d}{d\theta} \left(\frac{\kappa^2}{2} \right) = \frac{-F}{EI} \sin\theta \quad (9)$$

Separating variables and integrating yields

$$\frac{\kappa^2}{2} = \frac{F}{EI} \cos\theta + C \quad (10)$$

The constant of integration, C , can be found by using the boundary conditions at the pinned end of the segment. At the pinned end there is no internal moment, so Eq. (2) becomes

$$\kappa(\theta = \theta_0) = \frac{1}{R_0} \quad (11)$$

Solving first for C , substituting C into Eq. (10), and rearranging yields

$$\kappa = \sqrt{\frac{2F}{EI} (\cos\theta - \cos\theta_0) + \frac{1}{R_0^2}} \quad (12)$$

Various transformations need to be performed on Eq. (12) to prepare it for the elliptic integral solution. First, three new variables are defined as

$$\kappa_0 = \frac{L}{R_0} \quad (13)$$

$$\alpha^2 = \frac{FL^2}{EI} \quad (14)$$

$$\lambda = \frac{\kappa_0^2}{2\alpha^2} - \cos\theta_0 \quad (15)$$

where κ_0 is the non-dimensionalized curvature at the free end of the segment, α^2 is the non-dimensionalized load factor, and λ is a parameter used to transform the equation to an elliptic integral form. By substituting Eqs. (13) to (15) and Eq. (4), Eq. (12) can be expressed as

$$\frac{d\theta}{ds} = \frac{\sqrt{2}\alpha}{L} \sqrt{\lambda + \cos\theta} \quad (16)$$

Separating variables and integrating gives

$$\alpha = \frac{1}{\sqrt{2}} \int_0^{\theta_0} \frac{d\theta}{\sqrt{\lambda + \cos\theta}} \quad (17)$$

Equation (17) has no elementary solution, but is in a form that can be solved with elliptic integrals as
for $\lambda > 1$

$$\alpha = tF(\beta, t) \quad (18)$$

for $|\lambda| < 1$

$$\alpha = F(\psi, r) \quad (19)$$

where

$$\beta = \frac{\theta_0}{2} \quad (20)$$

$$t = \sqrt{\frac{2}{\lambda + 1}} \quad (21)$$

$$\psi = \text{asin} \sqrt{\frac{1 - \cos\theta_0}{\lambda + 1}} \quad (22)$$

$$r = \sqrt{\frac{\lambda + 1}{2}} \quad (23)$$

and $F(\beta, t)$ and $F(\psi, r)$ are incomplete elliptic integrals of the first kind.

Both Eqs. (18) and (19) have restrictions governing the valid ranges for their usage. These are

$$0 < \theta_0 \leq \pi \quad \text{for Eq. (18)} \quad (24)$$

$$0 < \theta_0 \leq \text{acos}(-\lambda) \quad \text{for Eq. (19)} \quad (25)$$

Knowing the value for α , equations can now be developed

for a and b , the x - and y -coordinates of the pin joint in the deflected position. The equation for the horizontal displacement a will be treated first. Using the relationship established in Eq. (7), an expansion of Eq. (4) results in

$$\kappa = \frac{d\theta}{ds} = \frac{d\theta dx}{dx ds} = \frac{d\theta}{dx} \cos\theta \quad (26)$$

Equation (16) can now be expressed in terms of x and θ as

$$\frac{d\theta}{dx} \cos\theta = \frac{\sqrt{2}\alpha}{L} \sqrt{\lambda + \cos\theta} \quad (27)$$

Separating variables and integrating along the length of the fixed-pinned beam gives the final form:

$$\frac{a}{L} = \frac{1}{\sqrt{2}\alpha} \int_0^{\theta_0} \frac{\cos\theta d\theta}{\sqrt{\lambda + \cos\theta}} \quad (28)$$

Once again, Eq. (28) is intractable and an elliptic integral solution must be used as follows:

for $\lambda > 1$

$$\frac{a}{L} = \frac{1}{\alpha t} [(t^2 - 2)F(\beta, t) + 2E(\beta, t)] \quad (29)$$

for $|\lambda| < 1$

$$\frac{a}{L} = \frac{1}{\alpha} [2E(\psi, r) - F(\psi, r)] \quad (30)$$

with β , t , ψ , and r as defined in Eqs. (20) to (23), and $E(\beta, t)$ and $E(\psi, r)$ being incomplete elliptic integrals of the second kind. The preceding relationships also have usage constraints. They are

$$\alpha \neq 0 \quad (31)$$

$$\lambda > -1 \quad (32)$$

$$0 < \theta_0 \leq \pi \quad \text{for Eq. (29)} \quad (33)$$

$$0 < \theta_0 \leq \text{acos}(-\lambda) \quad \text{for Eq. (30)} \quad (34)$$

The equations for non-dimensionalized b follow a slightly different derivation. Expanding Eq. (4) in terms of y instead of x ,

$$\kappa = \frac{d\theta}{ds} = \frac{d\theta dy}{dy ds} = \frac{d\theta}{dy} \sin\theta \quad (35)$$

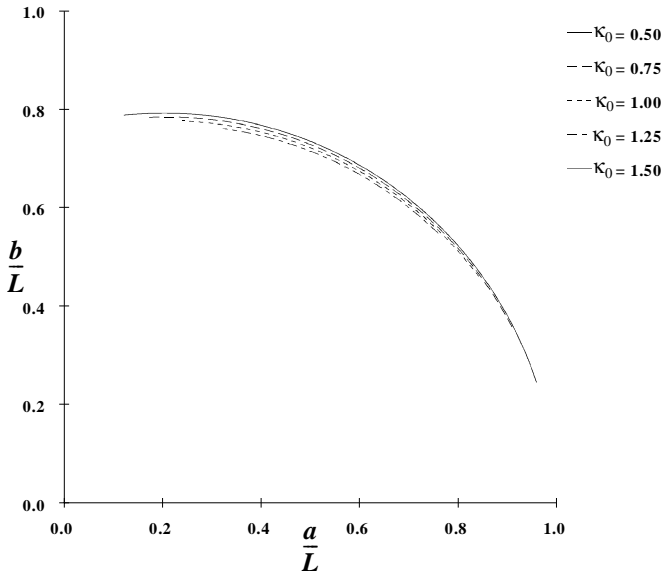


Figure 6: $\frac{a}{L}$ vs. $\frac{b}{L}$ at various κ_0 values

This allows Eq. (16) to be rewritten and integrated in terms of y and θ :

$$\frac{b}{L} = \frac{1}{\sqrt{2}\alpha} \int_0^{\theta_0} \frac{\sin \theta d\theta}{\sqrt{\lambda + \cos \theta}} \quad (36)$$

The integral in Eq. (36) may be solved through trigonometric substitution. The final equation is

$$\frac{b}{L} = \frac{\sqrt{2}}{\alpha} (\sqrt{\lambda + 1} - \sqrt{\lambda + \cos \theta_0}) \quad (37)$$

The constraints on Eq. (37) are

$$\alpha \neq 0 \quad (38)$$

$$\lambda > -\cos \theta_0 \quad (39)$$

With equations developed for the force-deflection characteristics of the FBPP half-segment, it is helpful to graph the segment deflection to aid in creating a simplified model. Assuming material constraints are not exceeded in bending, Fig. 6 presents the deflection characteristics for the beam tip at various values of κ_0 . As evidenced in Fig. 6, the deflection curves are nearly circular, although not about the origin. This information will be used in the next section to develop a simplified, pseudo-rigid-body model for FBPP segments.

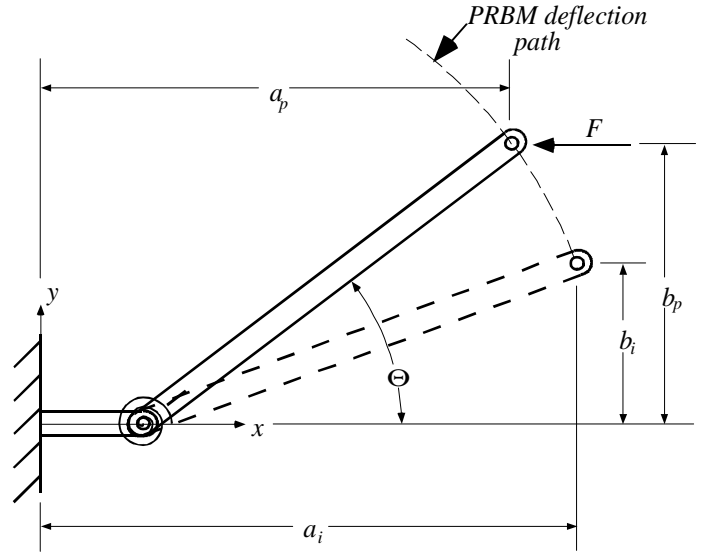


Figure 7: PRBM in deflected position

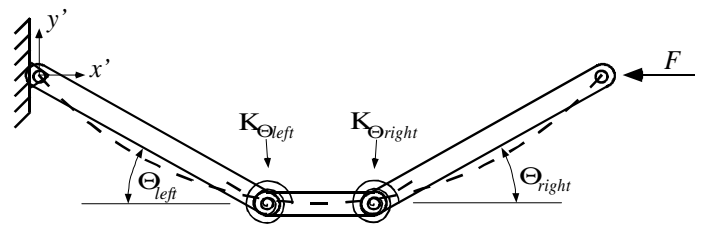


Figure 8: PRBM for entire FBPP segment

THE PSEUDO-RIGID-BODY MODEL

The elliptic integral solution for the deflection of the half-model shows a near-circular path for the end of the half-segment. Using this concept, a simplified model, called the pseudo-rigid-body model (PRBM), can be developed to facilitate the force-deflection calculations for functionally binary pinned-pinned (FBPP) segments. This model, shown in Fig. 7, uses two rigid links and a torsional spring to approximate the original nonlinear bending characteristics of the FBPP segment, with the link lengths and spring constant dependent on the initial curvature of the segment. The torsional spring models the segment's bending stiffness, and is placed at the center of the circular deflection path shown in Fig. 6.

Note that, due to symmetry, the half-model is equally applicable to either side of the FBPP segment. Thus the entire FBPP segment shown in Fig. 2 may be represented in terms of an identical PRBM on each side of the segment midpoint. The resulting rigid-body model is given in Fig. 8. The PRBM on the left is coupled with the PRBM on the right side of the segment midpoint by requiring the two angles θ_{left} and θ_{right} to be equal in value, as well as the torsional spring constants $K_{\theta_{left}}$ and $K_{\theta_{right}}$. Likewise, the lengths of the corresponding rigid links

for each PRBM must be equal in value. The link lengths and torsional spring characteristics of the half-segment PRBM are developed in the following sections. The predictions of the PRBM for the half-segment will then be compared to measurements from physical FBPP segments.

Derivation of the PRBM Link Lengths

For the PRBM given in Fig. 7, it is apparent that the key factor governing accurate endpoint deflection approximations is obtaining the correct lengths for the two rigid links. The length of the fixed link is defined by the non-dimensionalized parameter γ , the “fundamental radius factor,” as $L(1-\gamma)$, where L is the length of the half-segment. However, since the beam is initially curved the second rigid link cannot have a length γL . If it did, the link would be too long to represent the actual endpoint of the curved beam. The length of the second link must be the radius of the circular motion path described in Fig. 6. A new parameter ρ is defined as the “characteristic radius factor,” with the distance ρL being the characteristic radius (Howell and Midha, 1996). The second link then has a length ρL , where ρ is defined from simple geometry as

$$\rho = \sqrt{\left(\frac{a_i}{L} - (1-\gamma)\right)^2 + \left(\frac{b_i}{L}\right)^2} \quad (40)$$

where a_i and b_i are the initial horizontal and vertical positions of the segment endpoint.

Since the initial locations of both the half-segment and PRBM endpoints are the same, the non-dimensionalized initial horizontal position, $\frac{a_i}{L}$, can be determined from known values as

$$\frac{a_i}{L} = \frac{1}{\kappa_0} \sin \kappa_0 \quad (41)$$

Similarly, the non-dimensionalized initial vertical endpoint position is

$$\frac{b_i}{L} = \frac{1}{\kappa_0} (1 - \cos \kappa_0) \quad (42)$$

Since the segment is initially curved, the angle the second link makes with the x -axis will be non-zero. This angle Θ , called the pseudo-rigid-body angle, has an initial value Θ_i of

$$\Theta_i = \tan^{-1}\left(\frac{b_i}{a_i - L(1-\gamma)}\right) \quad (43)$$

Upon application of a force F , the PRBM deflects to the position

shown in Fig. 7. The new value of Θ is given by

$$\Theta = \tan^{-1}\left(\frac{b_p}{a_p - L(1-\gamma)}\right) \quad (44)$$

with a_p and b_p being the new horizontal and vertical coordinates of the PRBM endpoint. If Θ is known, the non-dimensionalized horizontal and vertical positions of the PRBM segment endpoint may be found from

$$\frac{a_p}{L} = 1 - \gamma + \rho \cos \Theta \quad (45)$$

and

$$\frac{b_p}{L} = \rho \sin \Theta \quad (46)$$

Given the two lengths for the rigid links, the PRBM endpoint path will stay within a specified error region (compared to the actual endpoint path) over a certain range of deflection. Thus the ideal PRBM is the one whose link lengths allow the largest range of deflection over which the error stays within the specified region. Because the fundamental radius factor, γ , determines the characteristic radius factor ρ , the deflection path depends only on γ . The solution method followed for obtaining the value of γ will be similar to that followed by Howell and Midha (1996).

At any two corresponding points on the PRBM and elliptic integral deflection curves, the relative error between the two paths is ϵ , where ϵ is defined to be

$$\epsilon = \frac{\sqrt{\left(\frac{a}{L} - \frac{a_p}{L}\right)^2 + \left(\frac{b}{L} - \frac{b_p}{L}\right)^2}}{\sqrt{\left(\frac{a}{L} - \frac{a_i}{L}\right)^2 + \left(\frac{b}{L} - \frac{b_i}{L}\right)^2}} \quad (47)$$

The error region is defined as a non-dimensionalized constant distance ϵ_{max} on either side of the PRBM deflection path. The error region is narrow near the undeflected initial position, and widens as the angle of deflection increases. Finally, a variable $(\Delta\Theta)_{max}$ is defined as

$$(\Delta\Theta)_{max} = \Theta_{max} - \Theta_i \quad (48)$$

where Θ_{max} is the value of the pseudo-rigid-body angle at which the PRBM approximation exceeds the error bound ϵ_{max} . $(\Delta\Theta)_{max}$ is then the difference between the initial angle of the rigid link and the final angle at which the error is exceeded.

The search for the optimal fundamental radius factor as a

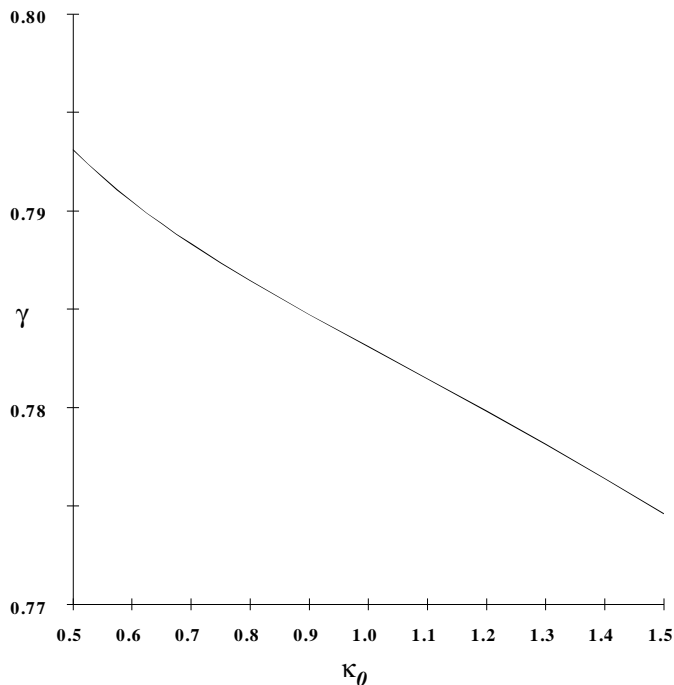


Figure 9: Optimized γ values at curvatures κ_0

function of κ_0 then resolves itself into the following one-dimensional problem:

Find the value of γ which maximizes deflection angle $(\Delta\Theta)_{max}$, where

$$\varepsilon \leq \varepsilon_{max} \text{ for } \Theta_i \leq \Theta \leq \Theta_{max} \quad (49)$$

The optimization method implemented for finding γ is the Golden Section method (Rao, 1984). For all cases, a parameter value of $\varepsilon_{max} = 0.5\%$ was utilized in the error calculations. The optimized values for γ over the range of $0.5 \leq \kappa_0 \leq 1.5$ are shown in Fig. 9. Table 1 shows the γ and ρ values at selected κ_0 values, with the corresponding $(\Delta\Theta)_{max}$ value for each curvature κ_0 .

As seen in Fig. 9, the κ_0 - γ graph has two nearly linear

Table 1: PRBM rigid link characteristics

κ_0	γ	ρ	$(\Delta\Theta)_{max}$
0.50	0.793	0.791	1.677
0.75	0.787	0.783	1.456
1.00	0.783	0.775	1.327
1.25	0.779	0.768	1.203
1.50	0.775	0.760	1.070

regions along the curvature range. Hence two linear least-squares curve fits describing γ in terms of κ_0 are

$$\gamma = 0.8063 - 0.0265\kappa_0 \quad 0.500 \leq \kappa_0 \leq 0.595 \quad (50)$$

$$\gamma = 0.8005 - 0.0173\kappa_0 \quad 0.595 \leq \kappa_0 \leq 1.500 \quad (51)$$

with a correlation coefficient $r^2 \geq 0.999$ in each case.

DERIVATION OF THE PRBM SPRING CONSTANT

The spring constant of the torsional spring needs to be ascertained to complete the modeling of the segment's stiffness. Norton (1991) and Howell et al. (1996) proposed stiffness coefficients for initially straight fixed-pinned segments, while Howell and Midha (1996) extended the theory to initially curved fixed-pinned segments subjected to variable-angle end forces. However, the case of pure horizontal loading has not been addressed by these authors. Since FBPP segments experience pure horizontal loading, a new stiffness analysis is required.

To avoid dimensional characteristics, the equation for the spring constant will be developed in non-dimensionalized terms. The horizontal applied force F may be expressed in non-dimensionalized form as α^2 , which is defined as

$$\alpha^2 = \frac{FL^2}{EI} \quad (52)$$

However, only part of the load F acts to rotate the rigid link. The component which is tangential to the link, F_t , actually deflects the link, while the axial component F_a has no effect on rotation. The tangential force is determined to be

$$F_t = F \sin \Theta \quad (53)$$

The non-dimensionalized tangential force α_t^2 is given by

$$\alpha_t^2 = \frac{F_t L^2}{EI} \quad (54)$$

Substituting Eq. (53) into Eq. (54) results in

$$\alpha_t^2 = \frac{FL^2 \sin \Theta}{EI} \quad (55)$$

or

$$\alpha_t^2 = \alpha^2 \sin \Theta \quad (56)$$

The deflection of the rigid link, $\Delta\Theta$, can be defined as the difference between the current pseudo-rigid-body angle and the

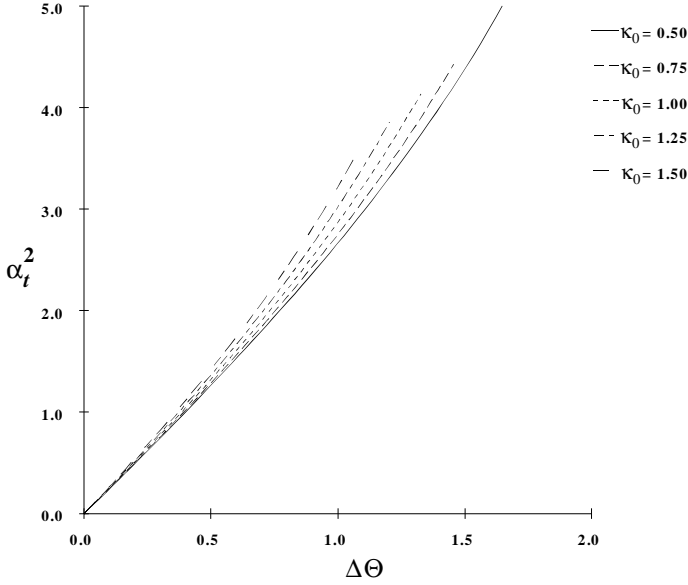


Figure 10: Force-deflection relationship at various κ_0

initial angle, or

$$\Delta\Theta = \Theta - \Theta_i \quad (57)$$

It remains, then, to determine a model describing the stiffness of the torsional spring. For various non-dimensionalized curvatures κ_0 , a graphical representation of the force-rotation deflection ($\alpha_t^2 - \Delta\Theta$) relationship is found in Fig. 10. Over the first portion of the graph, the slope of each of the curves is nearly constant. Therefore, it may be modeled by a linear relationship as

$$\alpha_t^2 = K_\Theta \Delta\Theta \quad (58)$$

where K_Θ is the spring stiffness coefficient.

The approximation was extended over the largest $\Delta\Theta$ range possible while keeping the correlation coefficient $r^2 \geq 0.999$. The relationship between K_Θ and κ_0 is illustrated in Fig. 11 over the range $0.5 \leq \kappa_0 \leq 1.5$. Table 2 contains the values of K_Θ for selected curvatures κ_0 .

If a simple equation is desired for quick calculations, the following relationship has a correlation coefficient $r^2 \geq 0.999$ and can be used to approximate the torsional spring constant for curvatures of $0.5 \leq \kappa_0 \leq 1.5$:

$$K_\Theta = 2.568 - 0.028\kappa_0 + 0.137\kappa_0^2 \quad (59)$$

The value of the torsional spring constant may be found using the equation

$$M = K\Delta\Theta = F_t \rho L \quad (60)$$

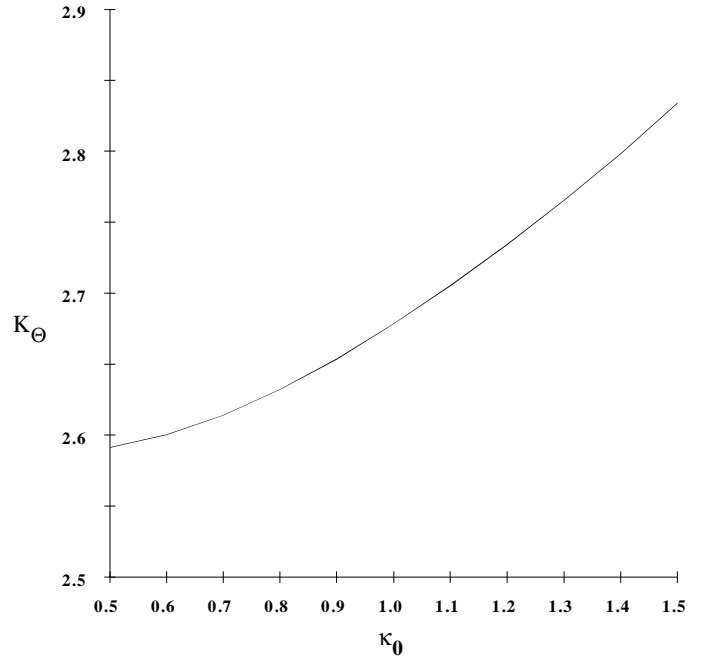


Figure 11: Torsional spring constant K_Θ as function of curvature

where M is the moment applied to the pin joint and K is the torsional spring constant. By combining Eq. (60) with Eqs. (54) and (58), the equation for K is found to be

$$K = \rho K_\Theta \frac{EI}{L} \quad (61)$$

When a larger $\Delta\Theta$ range is required, a second-order curve fit will accurately model the force-rotation relationship over the entire range that the PRBM deflection path is accurate. Similar to Eq. (58), it will be of the form

$$\alpha_t^2 = K_{\Theta 1} \Delta\Theta + K_{\Theta 2} (\Delta\Theta)^2 \quad (62)$$

Table 2: Torsional Spring Constant Characteristics

κ_0	K_Θ	$(\Delta\Theta)_{max}$
0.50	2.59	0.99
0.75	2.62	0.86
1.00	2.68	0.79
1.25	2.75	0.71
1.50	2.83	0.63

The values for $K_{\Theta 1}$ and $K_{\Theta 2}$ at various curvatures are shown in Table 3. The equation for the spring function $K(\Delta\Theta)$ may be found using the approach used above for the first-order curve fit. It is

$$K(\Delta\Theta) = \rho \frac{EI}{L} (K_{\Theta 1} + K_{\Theta 2} \Delta\Theta) \quad (63)$$

VALIDATION OF THE PRBM

To verify the PRBM theory for FBPP segments, various physical segments were machined for use in testing. Test mechanisms were created from A36-mild steel, 6061-T651 aluminum, and polypropylene, with the flexural rigidities (EI) being different in each case. To ensure that the resulting data was independent of the direction of deflection, two separate tests were performed on each segment. In the first, incremental forces were applied to the segment from an initially undeflected position, while the second test started with the segment in the deflected position and incrementally decreased the applied force.

The equations for the PRBM spring constant previously developed allowed for either a first or second order relationship between the change in pseudo-rigid-body angle $\Delta\Theta$ and the non-dimensionalized force parameter α_t^2 . Thus, for each mechanism two different predicted values are obtained, one from each of the PRBM approximations.

There are two important relationships which must be analyzed to validate the PRBM equations for FBPP segments: the deflection path and the force-deflection relationship. In each case, the results from the elliptic integral solution and the physical mechanism data are compared against the predicted values obtained from the PRBM. Appropriate transformations were made to convert the physical data into the half-model form required for comparison against the elliptic integral and PRBM solutions. Each mechanism was subjected to a series of tests, with the force-deflection data being averaged for each separate material type to obtain a truer relationship. The deflection path and force-deflection relationship for the aluminum segments are found in Figures 12 and 13. These two plots are representative of the results obtained for the aluminum, mild steel, and polypro-

Table 3: Second-order spring constant characteristics

κ_0	$K_{\Theta 1}$	$K_{\Theta 2}$	$(\Delta\Theta)_{max}$
0.50	2.24	0.46	1.68
0.75	2.30	0.48	1.46
1.00	2.34	0.55	1.33
1.25	2.40	0.64	1.20
1.50	2.48	0.73	1.07

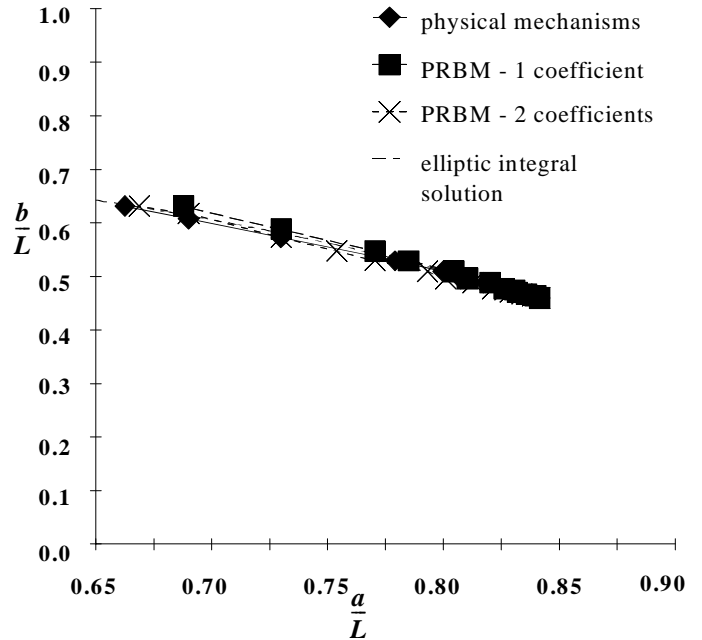


Figure 12: Aluminum deflection path for $\kappa_0 = 1.0$

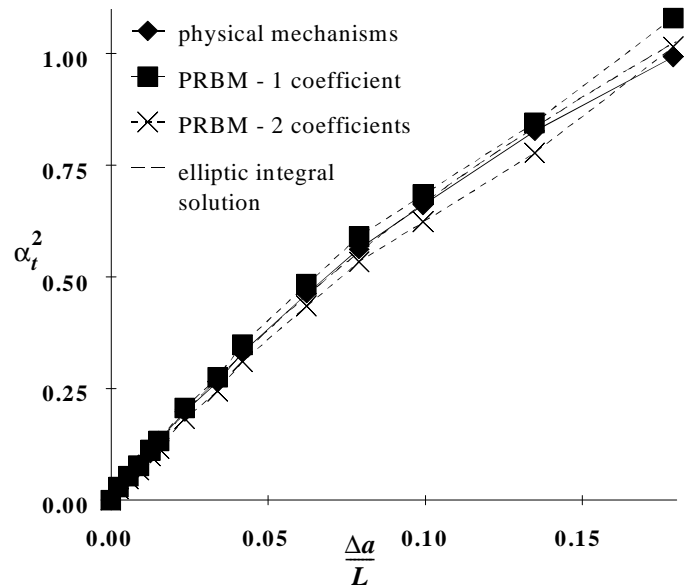


Figure 13: Aluminum force-deflection relationship for $\kappa_0 = 1.0$

pylene segments (Edwards, 1996).

The plot of the deflection paths shows a close approximation of the PRBM equations to the actual physical segments, while more error is evident in the force-deflection curves. The error found in the force-deflection curves is attributed to various sources. Since it is important when analyzing elastic behavior to avoid undergoing high stresses which may cause plastic yielding, the segments were designed to have relatively small force requirements. However, this caused the force data to fall

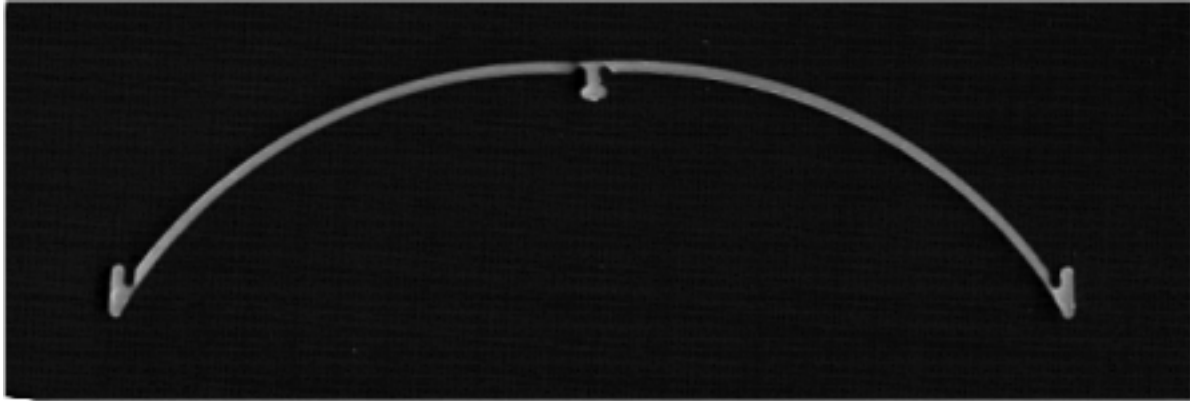


Figure 14: Bistable CD ejection actuator

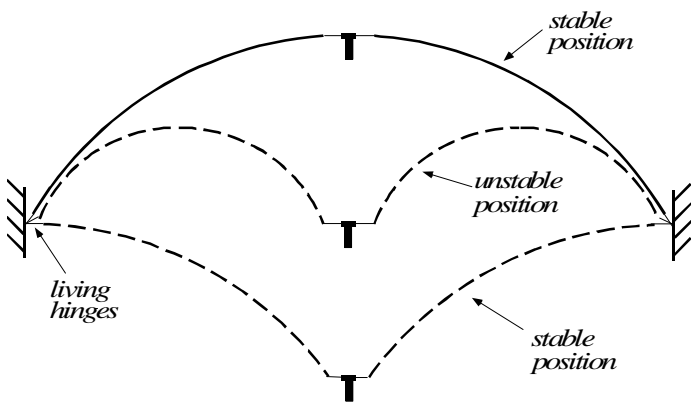


Figure 15: Stable and unstable equilibrium positions

into the range of the least-count of the force transducer used in the measurements, introducing a large uncertainty region for the forces. Also, frictional forces occurring principally at the pin joints have an effect on the force readings, but do not influence the positional data. Finally, stresses and discontinuities introduced during the fabrication of the physical segments also produce unknown effects on the behavior of the test mechanisms. These elements have a greater impact on the force-deflection relationship than on the deflection path of the segments.

EXAMPLE

The bistable CD ejection actuator shown in Fig. 14 is an example of a compliant mechanism using FBPP segments. This mechanism has one unstable and two stable equilibrium positions as shown in Fig. 15. The actuator is composed of two flexible members joined at each end by living hinges (flexural pivots with very little stiffness). The flexible members are identical in length and flexural rigidity (EI), and the deflection paths are constrained to be the same about the vertical plane

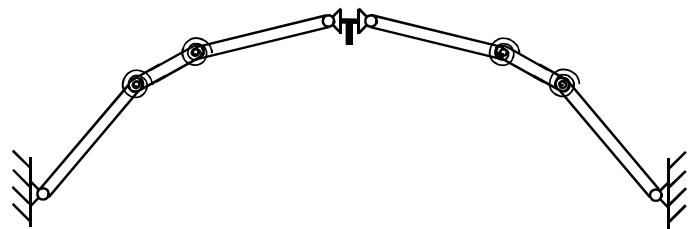


Figure 16: PRBM for entire actuator

halfway between the two fixed ends. The actuator serves as a medium for the storage and retrieval of a multimedia disk, such as a compact disk. The width of the two flexible beams is 1.22 mm, and the thickness out of the plane is 3.23 mm.

Living hinges can be modeled as being equivalent to pin joints at the same locations. Hence the actuator may be represented by a mechanism with each of the flexural pivots being replaced by pin joints. The actuator now can be seen to be two FBPP segments fixed at the opposing ends, and joined at the common end by the same pin joint. The PRBM for the entire actuator is given in Fig. 16.

Since both the FBPP segments rotate as the actuator is deflected, a constant applied vertical force will have a varying axial effect on the deflection of the segments. Consider the two equilibrium positions for a single FBPP segment shown in Fig. 17. At the top position, the force F has the axial and tangential components F_a and F_t , respectively. F_a is the only component which acts to deflect the segment, with F_t causing the rotation. In the second (unstable) state, the force F has no axial component, and thus a pure rotational force F_t occurs as the actuator deflects through this position. The variation of the axial component F_a during deflection may be approximated by using the equation $F_a = F \cos \beta$, with the angle β as defined in Fig. 17.

The equilibrium positions of the flexible FBPP segments are shown in Fig. 18, where the stable equilibrium states have been rotated to facilitate the analysis. Since the two stable equilibrium positions have identical FBPP segment shapes, the force F_{max}

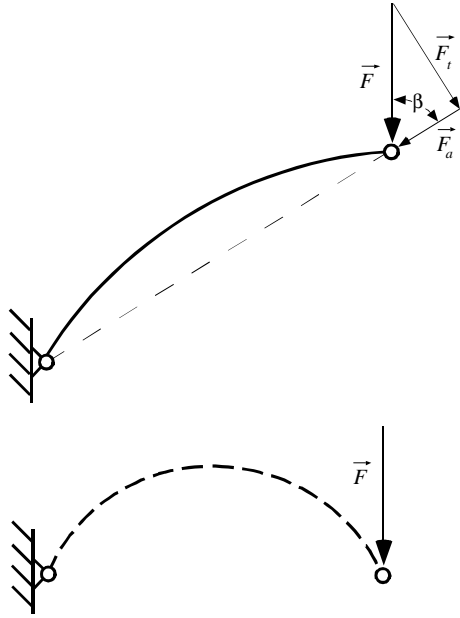


Figure 17: Axial force component F_a and tangential force component F_t

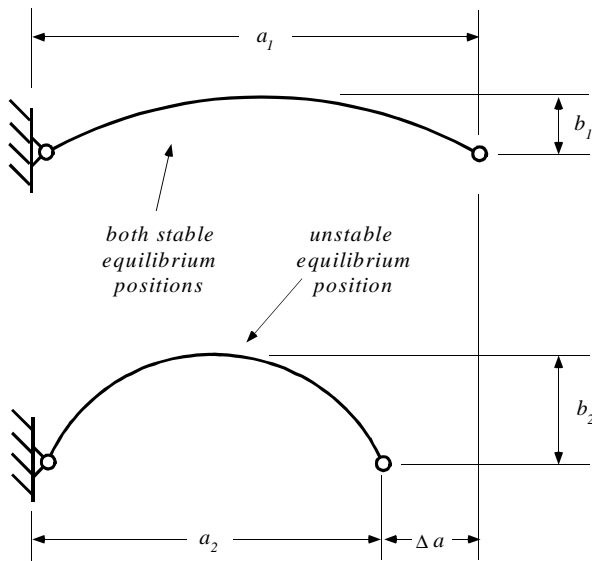


Figure 18: Determination of horizontal and vertical deflections

required to push the actuator from either stable position to the unstable state will be the same in either direction. The axial deflection Δa and vertical midpoint deflection Δb occurring upon deflection from the stable to the unstable position are given by

$$\Delta a = a_1 - a_2 \quad (64)$$

$$\Delta b = b_2 - b_1 \quad (65)$$

The predicted value for F_{max} was determined using the PRBM approximation, based on the dimensional characteristics of the actuator. Each of the FBPP segments has an initial radius of curvature $R_0 = 55.6$ mm, a segment length $L' = 63.0$ mm, and a half-model length $L = 31.5$ mm. Thus the non-dimensionalized curvature of each half-segment is $\kappa_0 = 0.57$. Using the methods described in the preceding sections, the PRBM parameter values for this curvature are calculated to be $\gamma = 0.7913$, $\rho = 0.7884$, $K_\Theta = 2.6233$, $K_{\Theta_1} = 2.2592$, and $K_{\Theta_2} = 0.4540$. These values were then input into the PRBM equations for the 1-coefficient and 2-coefficient torsional spring constants, which output the corresponding predicted values for the toggle force F_{max} .

The force and deflection values obtained for the actuator are shown in Table 4, along with the predicted force values based on the 1-coefficient and 2-coefficient torsional spring constant equations. Considering that the least count of the force transducer is 0.02 N., the force F measured by the transducer is well within a reasonable range of accuracy for the 2-coefficient PRBM approximation. The 1-coefficient approximation is also observed to perform reasonably well.

CONCLUSION

Functionally binary pinned-pinned segments are a common part of many compliant mechanisms. Because of their non-linear deflection behavior, however, prediction of FBPP segment deflection has been difficult in the past. Therefore, FBPP segments have been analyzed in this paper to determine their force-deflection characteristics. Elliptic integral solutions were used to develop analytic expressions for FBPP segment motion. Using these solutions, a pseudo-rigid-body model was developed to allow easier modeling of FBPP segments. This model represents the FBPP half-segment as two rigid beams joined by a pin joint. A torsional spring at the pin joint models segment stiffness. The force-deflection characteristics of the segment are modeled by choosing appropriate link lengths as well as the torsional spring constant. The accuracy of the model was tested using test segments fabricated from aluminum, steel, and polypropylene. In each case, the model accurately predicted the segments' force-deflection characteristics. An example mechanism using FBPP

Table 4: Force and deflection values for actuator at $\Delta a = 2.64$ mm, $\Delta b = 2.77$ mm

	F_{max}	α_{max}^2
actuator	0.534 N	0.791
PRBM - 1 Coefficient	0.596 N	0.884
PRBM - 2 Coefficients	0.529 N	0.786

segments was also analyzed, and the model proved useful in predicting its motion.

ACKNOWLEDGMENTS

Thanks is given to Compliant Solutions, who allowed the use of the bistable CD ejection actuator. This material is based upon work supported under a National Science Foundation Graduate Fellowship and a National Science Foundation Career Award No. DMI-9624574.

REFERENCES

Ananthasuresh, G.K., and Kota, S., 1994, "A Methodical Approach to the Design of Compliant Micromechanisms," *Solid-State Sensor and Actuator Workshop*, Hilton Head Island, south Carolina, pp. 189-192.

Ananthasuresh, G.K. and Kota, S., 1995, "Designing Compliant Mechanisms," *Mechanical Engineering*, Vol. 117, No. 11, pp. 93-96.

Bisshopp, K.E. and Drucker, D.C., 1945, "Large Deflection of Cantilever Beams," *Quarterly of Applied Mathematics*, Vol. 3, No. 3, pp. 272-275.

Byrd, P.F. and Friedman, M.D., 1954, *Handbook of Elliptic Integrals for Engineers and Physicists*, Springer-Verlag, Berlin.

Edwards, B.T., 1996, "Functionally Binary Pinned-Pinned Segments," MS Thesis, Brigham Young University, Provo, UT.

Frecker, M., Kota, S., and Kikuchi, N., 1997, "Use of Penalty Function in Topological Synthesis and Optimization of Strain Energy Density of Compliant Mechanisms," *Proceedings of DETC'97, ASME Design Engineering Technical Conferences, DETC97/DAC-3760*.

Frisch-Fay, R., 1962, *Flexible Bars*, Butterworth, Washington, D.C.

Howell, L.L. and Midha, A., 1994, "A Method for the Design of Compliant Mechanisms with Small-Length Flexural Pivots," *ASME Journal of Mechanical Design*, Vol. 116, No. 1, pp. 280-290.

Howell, L.L. and Midha, A., 1995, "Parametric Deflection Approximations for End-Loaded, Large-Deflection Beams in Compliant Mechanisms," *ASME Journal of Mechanical Design*, Vol. 117, No. 1, pp. 156-165.

Howell, L.L. and Midha, A., 1996, "Parametric Deflection Approximations for Initially Curved, Large-Deflection Beams in Compliant Mechanisms," *Proceedings of the 1996 ASME Design Engineering Technical Conferences, 96-DETC/MECH-1215*.

Howell, L.L., Midha, A., and Norton, T.W., 1996, "Evaluation of Equivalent Spring Stiffness for Use in a Pseudo-Rigid-Body Model of Large-Deflection Compliant Mechanisms," *ASME Journal of Mechanical Design*, Vol. 118, No. 1, pp. 126-131.

King, L.V., 1924, *On the Direct Numerical Calculation of Elliptic Functions and Integrals*, Cambridge University Press, London.

Norton, T.W., 1991, "On the Nomenclature and Classification, and Mobility of Compliant Mechanisms," M.S. Thesis, Purdue University, West Lafayette, Indiana.

Rao, S.S., 1984, *Optimization: Theory and Applications*, Wiley Eastern Limited, New Delhi.

Sigmund, O., 1996, "On the Design of Compliant Mechanisms Using Topology Optimization," *Danish Center for Applied Mathematics and Mechanics*, Technical University of Denmark, Report No. 535.

Shoup, T.E. and McLarnan, C.W., 1971, "A Survey of Flexible Link Mechanisms Having Lower Pairs," *Journal of Mechanisms*, Vol. 6, No. 3, pp 97-105.